Peer-reviewed version available at *Photonics* **2018**, *5*, 48; doi:10.3390/photonics5040048

Type of the Paper (Article)

Comparative Modeling of Infrared Fiber Lasers

S. Sujecki[1,2*], L. Sojka[1], A.B. Seddon[2], T.M. Benson[2], E. Barney[2], M.C. Falconi[3], F. Prudenzano[3], M. Marciniak[4], H. Baghdasaryan[5], P. Peterka[6] and S. Taccheo[7]

[1] Wroclaw University of Science and Technology, Wyb. Wyspianskiego 27, Wroclaw, Poland, 50-370
[2] The University of Nottingham, Nottingham, University Park, Nottingham, UK, NG7 2RD
[3] Politecnico di Bari, Bari, Via Edoardo Orabona, 4, Bari, Italy, 70125
[4] National Institute of Telecommunication, Szachowa 1, Warsaw, Poland, 04-894
[5] National Polytechnic University of Armenia, Teryan Str. 105, Yerevan, Armenia, 0009
[6] Institute of Photonics and Electronics, Czech Academy of Sciences, Chaberska 57, Prague, Czech Republic, 18251
[7] Laser Group, College of Engineering, Bay Campus, SA1 8EN Swansea, UK
* Correspondence: slawomir.sujecki@pwr.edu.pl; Tel.: +48-71-320-4588

Abstract: Modeling and design of fiber lasers facilitate the process of their practical realization. Of particular interest during the last few years is the development of lanthanide ion-doped fiber lasers which operate at wavelengths exceeding 2000 nm. There are two main host glass materials considered for this purpose, namely fluoride and chalcogenide glasses. Therefore, this study concerns comparative modeling of fiber lasers operating within the infrared wavelength region beyond 2000 nm. In particular, the convergence properties of selected algorithms, implemented within various software environments, are studied with a specific focus on the central processing unit (CPU) time and calculation residual. Two representative fiber laser cavities are considered: one is based on a chalcogenide-selenide glass step-index fiber doped with trivalent dysprosium ions whilst the other is a fluoride step-index fiber doped with trivalent erbium ions. The practical calculation accuracy is also assessed by comparing directly the results obtained from the different models.

Keywords: mid-infrared light sources; near-infrared light sources; rare earth-doped fibers

1. Introduction

Due to many potential applications in medicine, biology, environmental monitoring and defense, a large research effort has been devoted to the development of fiber lasers operating at wavelengths exceeding 2000 nm. Currently available light sources for these wavelengths include gas lasers, quantum cascade lasers, inter-band cascade lasers, supercontinuum fiber sources, Raman fiber lasers, light emitting diodes, optical parametric oscillators, the Globar©-type black-body sources and lanthanide ion-doped fiber lasers. A particular advantage of lanthanide ion-doped fiber lasers is their high output beam quality and compact structure; so far, such fiber lasers have only been demonstrated at wavelengths < 4000 nm [1,2]. Very recently a room temperature fiber laser operation up to 3920 nm has been demonstrated [3]. For operating wavelengths of up to 2000 nm, silica glass fiber based lasers can be used [4]. Fiber lasers operating at wavelengths from 2000 nm to 4000 nm are based on fluoride glass fibers; lanthanide ions that have been so far applied for doping fluoride glass fibers include erbium (III), holmium (III) and dysprosium (III) [5-12]. For the development of lanthanide ion-doped fiber lasers operating at wavelengths exceeding 4000 nm, the introduction of lower phonon energy glasses is required. Particularly good candidates for this purpose are chalcogenide glasses. Chalcogenide glasses have been shown to have sufficiently good mechanical properties, chemical stability towards water and oxygen, low loss at the relevant wavelengths, good solubility for lanthanide ions and can be drawn into fibers [13-36]. Thus, both chalcogenide and fluoride glasses have been intensely studied, both experimentally and theoretically, for applications in fiber lasers [20,37-42].

Peer-reviewed version available at Photonics 2018, 5, 48; doi:10.3390/photonics5040048

A vital element in the development process of fiber lasers reaching long operating wavelengths is their design. Design tools are needed for the optimization of laser parameters so that a lasing action under optimal conditions can be successfully achieved. Therefore, the properties of various numerical algorithms, applicable to the design and modeling of fiber lasers operating at wavelengths exceeding 2000 nm, are compared in this contribution. In particular, the optical characteristics of a dysprosium ion-doped chalcogenide glass fiber laser and an erbium ion-doped fluoride glass fiber laser were numerically studied. For this purpose, several algorithms developed within various software environments were compared. The dependence of the central processing unit (CPU) time and calculation residual on the iteration number was used to assess the convergence properties of individual algorithms.

2. Materials and Methods

Fig.1 shows the configuration of the fiber laser cavity considered. The pump light is applied at one end of the fiber, whilst the signal and idler waves are collected at the other end of the fiber.

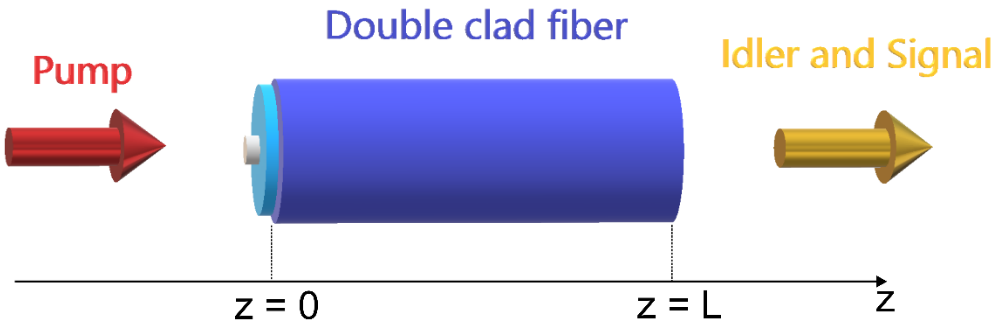

Figure 1. Schematic diagram of the fiber laser cavity.

Two types of fibers were considered. The first one was a chalcogenide glass fiber core doped with trivalent dysprosium ions whilst the other one was a fluoride fiber core doped with trivalent erbium ions. The energy level diagram for dysprosium ions, here doped into a chalcogenide-selenide glass, is shown in Fig.2. The pump laser operating at 1710 nm populates level 2. It is assumed simplistically that neither significant up-conversion, nor excited state absorption, take place, so that only the three lowest lying energy levels must be included in the model. From energy level 2, a transition can take place to level 1 either through the process of spontaneous or stimulated emission, thus generating signal photons. Analogous transitions can take place between energy levels 1 and 0 accompanied by emission of idler photons. Due to the relatively long lifetime of energy level 1 measured experimentally [29], the inclusion of an idler is essential for obtaining efficient laser action. Note that the idler wave is trapped within the cavity, with the help of high reflectivity mirrors, and used to depopulate level 1. Using the energy level diagram shown in Fig.2, and the rate equation approach, one can write the following set of coupled algebraic equations that allow for the calculation of the energy level populations for dysprosium ions:

$$\begin{bmatrix} a_{11} & a_{12} & a_{13} \\ a_{21} & a_{22} & a_{23} \\ 1 & 1 & 1 \end{bmatrix} * \begin{bmatrix} N_0 \\ N_1 \\ N_2 \end{bmatrix} = \begin{bmatrix} 0 \\ 0 \\ N_{Dy} \end{bmatrix}, \tag{1}$$

whereby the sum of level populations N_0, N_1 and N_2 is equal to the total doping concentration N_{Dy}, and the coefficients a_{mn} are given by:

$$\begin{aligned} &a_{11}=\sigma_{pa}\ \phi_p;\quad a_{12}=\sigma_{sa}\ \phi_s;\quad a_{13}=-\sigma_{pe}\ \phi_p-\sigma_{se}\ \phi_s-\frac{1}{\tau_2}\\ &a_{21}=\sigma_{ia}\ \phi_i;\quad a_{22}=-\sigma_{ie}\ \phi_i-\sigma_{sa}\ \phi_s-\frac{1}{\tau_1};a_{23}=\sigma_{se}\ \phi_s+\frac{\beta_{21}}{\tau_2}\end{aligned}, \tag{2}$$

In (2) σ_{xa} is the absorption cross section for signal: s, idler: i and pump: p, while σ_{xe} gives the respective values for emission cross section. ϕ_x is the photon flux for signal: *s*, idler: *i* and pump: *p*. β_{21} is the branching ratio for the 2-1 transition (Fig.2), τ_1 and τ_2 are the radiative lifetimes for levels 1 and 2, respectively (Fig.2). The rate equations (1) are complemented by the set of six ordinary differential equations that describe the spatial evolution of the pump, idler and signal powers for both the forward and backward propagating waves along the z axis:

$$\begin{aligned} \frac{dP_p^{\pm}}{dz}&=\mp\Gamma_p\left[\sigma_{pa}N_0-\sigma_{pe}N_2\right]P_p^{\pm}\mp\alpha\ P_p^{\pm}\\ \frac{dP_s^{\pm}}{dz}&=\mp\Gamma_s\left[\sigma_{sa}N_1-\sigma_{se}N_2\right]P_s^{\pm}\mp\alpha\ P_s^{\pm}\quad,\\ \frac{dP_i^{\pm}}{dz}&=\mp\Gamma_i\left[\sigma_{ia}N_0-\sigma_{ie}N_1\right]P_i^{\pm}\mp\alpha\ P_i^{\pm}\end{aligned} \tag{3}$$

where Γ_x is the confinement factor for signal –*s*, idler –*i* and pump –*p*, α gives the loss coefficient and P_p, P_s and P_i are the values of power of the pump, signal and idler, respectively. A more rigorous approach, which does not use the confinement factor approximation, involves the exact calculation of the overlapping integrals between the ion populations and the electromagnetic field, by taking into account the spatial distribution of the optical propagation modes:

$$\begin{aligned} \frac{dP_p^{\pm}}{dz}&=\mp P_p^{\pm}\int_{A_d}\left[\sigma_{pa}N_0-\sigma_{pe}N_2\right]i_p dA\mp\alpha\ P_p^{\pm}\\ \frac{dP_s^{\pm}}{dz}&=\mp P_s^{\pm}\int_{A_d}\left[\sigma_{sa}N_1-\sigma_{se}N_2\right]i_s dA\mp\alpha\ P_s^{\pm}\quad,\\ \frac{dP_i^{\pm}}{dz}&=\mp P_i^{\pm}\int_{A_d}\left[\sigma_{ia}N_0-\sigma_{ie}N_1\right]i_i dA\mp\alpha\ P_i^{\pm}\end{aligned} \tag{4}$$

where A_d is the rare earth-doped region and i_p, i_s and i_i are the normalized intensities of the pump, signal and idler optical modes, respectively.

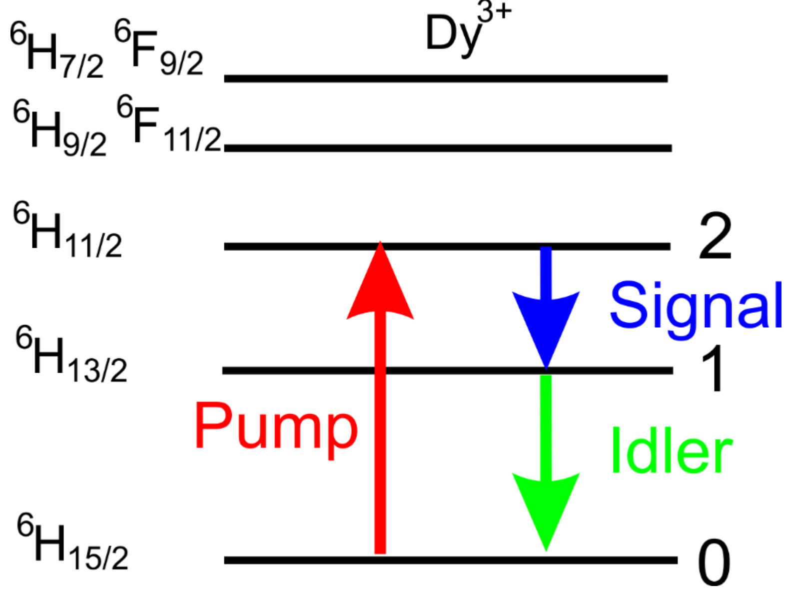

Peer-reviewed version available at *Photonics* **2018**, *5*, 48; doi:10.3390/photonics5040048

Figure 2. Energy level diagram of trivalent dysprosium ions.

Fig.3 shows the energy level diagram of erbium trivalent ions doped into fluoride glass. The pump operating at 980 nm promotes ions from the ground state to energy level 2. Also, via excited state absorption and co-operative up-conversion, the ions are promoted to energy level 3. The signal operates at 2800 nm wavelength and is amplified through interaction with energy levels 1 and 2. The idler signal may operate at approximately 1550 nm and interact with energy levels 0 and 1. In this model, however, it is assumed that the idler signal does not build up due to the cavity loss encountered. It is noted that in the fluoride fiber laser cavity considered, the inclusion of an idler is not needed for efficient laser action. From the Er^{3+} energy level diagram in Fig.3, using the rate equations' approach, one obtains consistently the following set of algebraic equations that enable calculation of the populations of the energy levels:

$$\begin{aligned}
&W_{22}N_2^2-\frac{N_4}{\tau_4}+R_{ESA}=0\\
&\frac{\beta_{43}N_4}{\tau_4}-\frac{N_3}{\tau_3}=0\\
&R_{GSA}-R_{SE}-R_{ESA}+\sum_{i=3}^{4}\frac{\beta_{i2}N_i}{\tau_i}-\frac{N_2}{\tau_2}-2W_{22}N_2^2+W_{11}N_1^2=0\,,\\
&R_{SE}+\sum_{i=2}^{4}\frac{\beta_{i1}N_i}{\tau_i}-\frac{N_1}{\tau_1}-2W_{11}N_1^2=0\\
&-R_{GSA}+\sum_{i=1}^{4}\frac{\beta_{i0}N_i}{\tau_i}+W_{22}N_2^2+W_{11}N_1^2=0
\end{aligned}\tag{5}$$

whereby the sum of level populations N_0, N_1, N_2, N_3, N_4, respectively, (Fig.3) is equal to the total doping concentration N_{Er}. Note that τ_1, τ_2, τ_3 and τ_4 are the life times of levels 1, 2, 3 and 4, respectively, while β_{xy} give the branching ratios from level x to y. W_{11} and W_{22} are the cooperative up-conversion coefficients for levels 1 and 2, respectively. R_{GSA} gives the ground state absorption rate, R_{SE} gives the rate of stimulated emission between levels 1 and 2, while R_{ESA} gives the rate of the excited state absorption from level 2 to level 4:.

$$R_{GSA}=\frac{\lambda_p\Gamma_p\sigma_{GSA}}{hcA_{eff}}N_0\left(P_p^{+}+P_p^{-}\right),\tag{6}$$

$$R_{SE}=\frac{\lambda_s\Gamma_s\sigma_{se}}{hcA_{eff}}\left(b_2N_2-\frac{g_2}{g_1}b_1N_1\right)\left(P_s^{+}+P_s^{-}\right),\tag{7}$$

$$R_{ESA}=\frac{\lambda_p\Gamma_p\sigma_{ESA}}{hcA_{eff}}N_2\left(P_p^{+}+P_p^{-}\right),\tag{8}$$

Equations (5) are complemented by a set of four ordinary differential equations, which describe the evolution of the pump and signal waves. The degeneracy parameters: $g_2 = g_1 = 2$. The values of the relevant cross sections σ_{se}, σ_{ESA} and σ_{GSA}, confinement factors Γ_x, wavelengths λ_x, effective cross section A_{eff} and Boltzmann factors b_x are given in Table 2. Aligning the fiber with the z axis of the coordinate system enables the following four differential equations to be written in the following form:

$$\begin{aligned}
&\frac{d}{dz}P_p^+ = -\Gamma_p\left(\sigma_{GSA}N_0+\sigma_{ESA}N_2\right)P_p^+ - \alpha_p P_p^+\\
&-\frac{d}{dz}P_p^- = -\Gamma_p\left(\sigma_{GSA}N_0+\sigma_{ESA}N_2\right)P_p^- - \alpha_p P_p^-\\
&\frac{d}{dz}P_s^+ = \Gamma_s\sigma_{SE}\left(b_2N_2-\left(g_2/g_1\right)b_1N_1\right)P_s^+ - \alpha_s P_s^+\\
&-\frac{d}{dz}P_s^- = \Gamma_s\sigma_{SE}\left(b_2N_2-\left(g_2/g_1\right)b_1N_1\right)P_s^- - \alpha_s P_s^-
\end{aligned}, \tag{9}$$

where: P_s and P_p are the powers of the signal and pump, respectively, and the superscripts '+' and '-' denote the forward and backward propagating waves, respectively. In equations (9), α_x gives the value of loss.

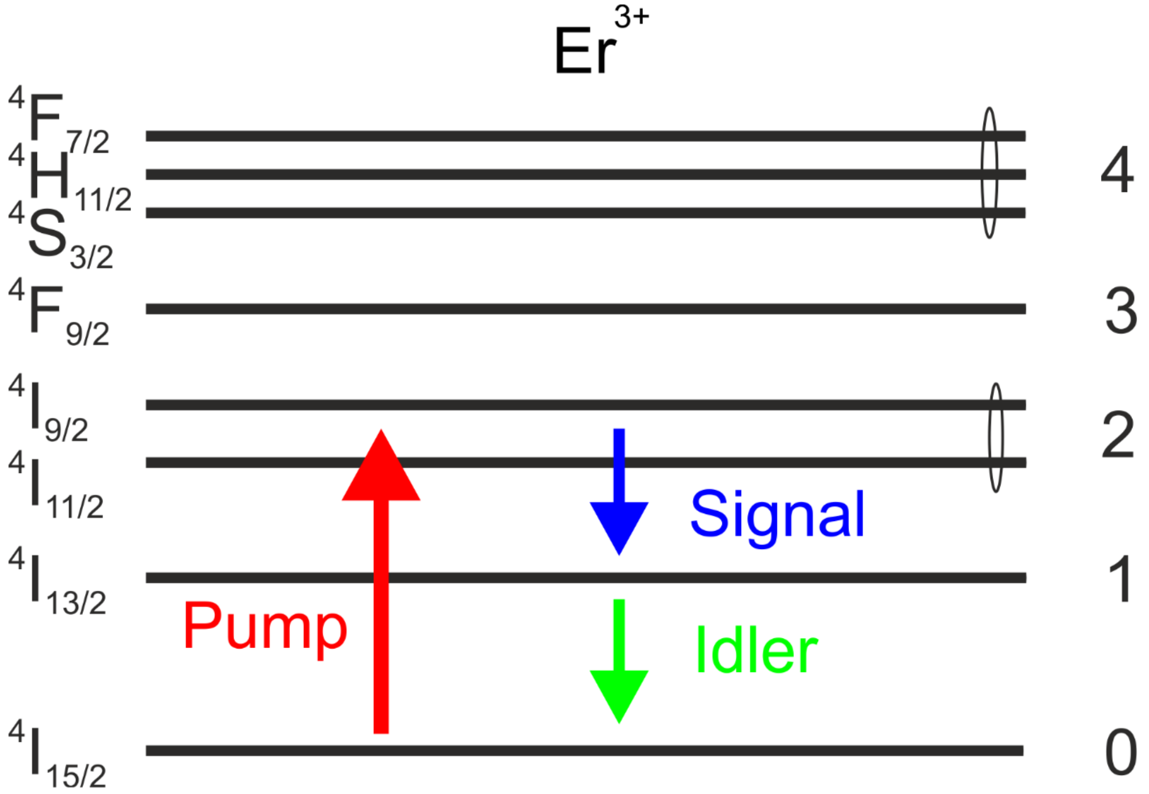

Figure 3. Energy level diagram of trivalent erbium ions.

The pump, signal and idler powers at the terminating end-fiber-faces of the laser cavity are subjected to the following boundary conditions:

$$\begin{aligned}
&P_p^+(z=0) = r_p(z=0)P_p^-(z=0) + \left[1-r_p(z=0)\right]P_{pump}\\
&P_p^-(z=L) = r_p(z=L)P_p^+(z=L)\\
&P^+(\lambda=\lambda_1, z=0) = r_{\lambda 1}(z=0)P^-(\lambda=\lambda_1, z=0)\\
&P^-(\lambda=\lambda_1, z=L) = r_{\lambda 1}(z=L)P^+(\lambda=\lambda_1, z=L)\\
&P^+(\lambda=\lambda_2, z=0) = r_{\lambda 2}(z=0)P^-(\lambda=\lambda_2, z=0)\\
&P^-(\lambda=\lambda_2, z=L) = r_{\lambda 2}(z=L)P^+(\lambda=\lambda_2, z=L)
\end{aligned}, \tag{10}$$

It should be noted that the boundary conditions (10) dictate the incident pump power, but not the value of the pump power after it has crossed the air-fiber end interface.

Three algorithms, developed by different research groups in different computational environments, are compared here. The main characteristics considered are the CPU time and the dependence of the calculation residual on the iteration number. The calculation residual is defined as the sum of the squared differences between values from the current and previous iteration, for signal, idler and pump, calculated at z=0. The CPU time was calculated using system functions. All three algorithms employed the relaxation method for solving the two-point boundary value problem, as follows:

- The UFE fiber laser model developed at the Institute of Photonics and Electronics of the Czech Academy of Sciences (UFE) has been implemented in C programming language (gcc 4.9.2) within the Windows 7 operating system, 64 bit Intel core i7-3930K CPU at 3.2 GHz. The UFE model is currently being developed for study of longitudinal-mode instabilities and associated build-up of dynamic fiber Bragg gratings (42).
- The PB fiber laser model developed at the Politecnico di Bari (PB) has been implemented in MATLAB within the Windows 10 operating system, 64-bit Intel Core i7-4790 CPU at 3.6 GHz. The numerical integration was carried out using a 4-5 Runge-Kutta algorithm and the more rigorous overlap integrals approach was employed.
- The NU-PWr fiber laser model developed at the University of Nottingham and Wroclaw University of Science and Technology (NU-PWr) has been implemented in MATLAB within the Windows 10 operating system, 64 bit Intel Core i5 7th Generation, CPU at 2.5 GHz. The numerical integration was carried out using a 4-5 Runge-Kutta algorithm.

3. Results

The modeling parameters for the dysprosium trivalent ion doped chalcogenide-selenide glass fiber laser are summarized in Table 1, while in Table 2 the modeling parameters for the erbium trivalent ion doped fluoride glass fiber laser are given.

Table 1 Numerical modeling parameters used in simulations Dy^{3+} doped chalcogenide glass fiber laser.

Quantity	unit	Value
Dy^{3+}ion concentration N_{Dy}	cm^{-3}	7×10^{19}
A_{eff}	m^2	95×10^{-12}
Fiber length L	m	2.1
Fiber loss at all wavelengths α	dB/m	1
Lifetime of level 2 (Fig.2)	ms	2
Lifetime of level 1 (Fig.2)	ms	5.2
Branching ratio for 2-1 transitions		0.15
Reflectivity for idler, signal and pump at $z = 0$		0.2
Reflectivity for idler, signal and pump at $z = L$		0.2
Confinement factor for signal		0.8
Confinement factor for idler		0.9

Confinement factor for pump		0.034
Pump wavelength	µm	1.71
Signal wavelength (λ_1)	µm	4.6
Idler wavelength (λ_2)	µm	3.35
Pump emission cross section	m^2	0.318×10^{-24}
Pump absorption cross section	m^2	0.501×10^{-24}
Signal emission cross section	m^2	0.912×10^{-24}
Signal absorption cross section	m^2	0.485×10^{-24}
Idler emission cross section	m^2	0.097×10^{-24}
Idler absorption cross section	m^2	0.016×10^{-24}

In the simulations, the value of Planck's constant of $6.62607004 \times 10^{-34}$ Js and the value of the speed of light in free space of 2.99792458×10^8 m/s were used.

Table 2 Numerical modeling parameters used in simulations Er^{3+} doped fluoride fiber laser.

Quantity	**unit**	**value**
b_1/b_2		0.1/0.16
W_{11}	m^3/s	1×10^{-24}
W_{22}	m^3/s	0.3×10^{-24}
σ_{GSA}	m^2	2.1×10^{-25}
σ_{SE}	m^2	4.5×10^{-25}
σ_{ESA}	m^2	1.1×10^{-25}
Γ_p		0.009
Γ_s		1.0
Er^{3+} ion concentration N_{Er}	m^{-3}	9.6×10^{26}
Pump wavelength λ_p	nm	976
Pump wavelength λ_s	nm	2800
Fiber length L	m	2.5

A_{eff}	m^2	314×10^{-12}
α_p	1/m	3×10^{-3}
α_s	1/m	23×10^{-3}
$R_p(z = 0)$		0
$R_p(z = L)$		0.04
$R_s(z = 0)$		0.96
$R_s(z = L)$		0.04

Table 3 shows the values of the relevant lifetimes and branching ratios for erbium trivalent ions, doped into a fluoride glass.

Table 3 Branching ratios and level lifetimes for erbium trivalent ions doped in a fluoride glass.

Quantity	**unit**	**value**
τ_1	ms	9
τ_2	ms	6.9
τ_3	ms	0.12
τ_4	ms	0.57
β_{21}, β_{20}		0.37, 0.63
β_{32}, β_{31}, β_{30}		0.856, 0.004, 0.14
β_{43}, β_{42}, β_{41}, β_{40}		0.34, 0.04, 0.18, 0.44

Fig.4 shows the dependence of the residual and the CPU time in the UFE model. The values of the CPU time show a step-wise behavior due to the quantization implemented within the C function clock which was used in the simulations. For the UFE model, the rate of residual reduction is smaller at low values of the output power. In particular, at an output power of 200 mW, one can observe that the residual decreases significantly more slowly than do the other three values of the output power.

Peer-reviewed version available at *Photonics* **2018**, *5*, 48; doi:10.3390/photonics5040048

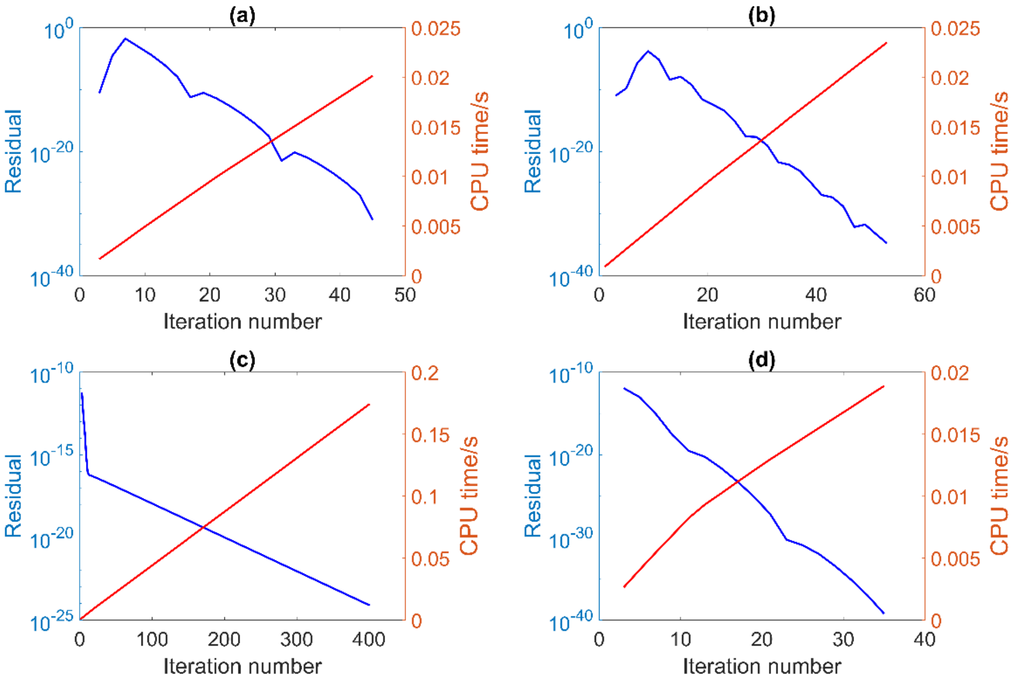

Figure 4. Dependence of the residual calculated using UFE model at z=0 and CPU time on the iteration number at pump power of: (a) 5 W, (b) 1 W, (c) 0.4 W and (d) 0.2 W.

An overall lower rate of the residual reduction in the case of the PB model, when compared with UFE model, is observed in the results shown in Fig.5. Also, the simulation time is at least three orders of magnitude larger despite the application of a faster processor at PB, which shows the advantage of direct C programming. Interestingly, the PB model shows a larger rate of residual decrease for low output powers. Fig.6 shows the results obtained with the NU-PWr model. When compared with the results obtained with PB model, one observes a much larger rate of residual reduction for NU-PWr model. The CPU time, in the PB model, when measured per iteration, is however less. The overall calculation time for the PB model had to reach a particular value of the residual, and this took a significantly longer time than the NU-PWr model. It is noted that for PB, the overlap integrals between the ion populations and the optical modes of pump, signal and idler are calculated over the rare earth-doped region according to equation (4). These integrals are updated along the fiber length, taking into account the ion population distributions. This causes a higher calculation time but allows higher solution accuracy.

Peer-reviewed version available at Photonics 2018, 5, 48; doi:10.3390/photonics5040048

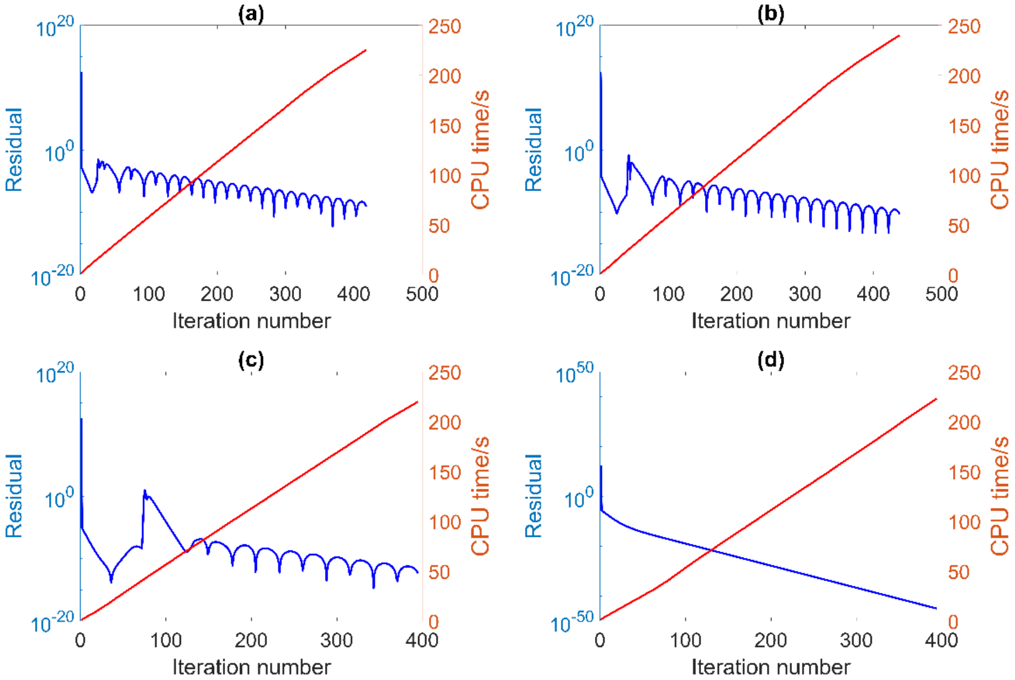

Figure 5. Dependence of the residual calculated using the PB model at z=0 and CPU time on the iteration number at pump power of: (a) 5 W, (b) 1 W, (c) 0.4 W and (d) 0.2 W.

Finally, in Tables 4-6 the results for the output power and the idler power, calculated using the UFE and the NU-PWr models, are compared for both the dysprosium trivalent ion doped chalcogenide glass fiber laser and the erbium trivalent ion doped fluoride glass fiber laser. For the Dy^{3+}-doped chalcogenide-selenide glass fiber laser, the results calculated using the UFE and the NU-PWr model the relative difference, defined as the ratio between the absolute value of the difference and half of the sum of the results, is then less than 0.2 % for the signal and below 0.22 % for the idler wave at pump powers of 1 W, and 5 W, respectively. In the case of the idler wave, the small values of the idler wave power for pump powers of 0.4 W, and 0.2 W, make it difficult to achieve small values of the relative difference. Nonetheless, these results consistently indicate that the idler is below the lasing threshold. In the case of the Er^{3+} doped fluoride glass fiber laser, both NU-PWr and UFE models calculated results agree on all 4 digits. It is noted that the results shown in Tables 4-6 were rounded to the nearest decimal.

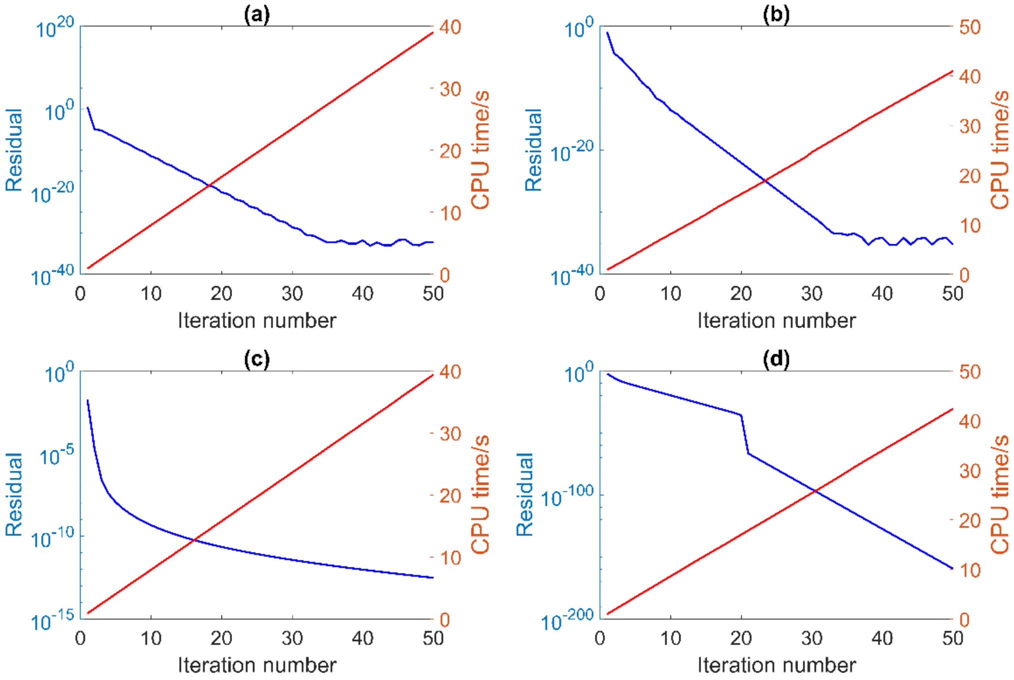

Figure 6. Dependence of the residual, calculated using the NU-PWr model at z=0, and CPU time on the iteration number at a pump power of: (a) 5 W, (b) 1 W, (c) 0.4 W and (d) 0.2 W.

Table 4 Calculated values of signal output power values for the Dy^{3+} doped chalcogenide-selenide glass fiber laser.

Pump power / W	Signal power (NU-PWr) / W	Signal power (UFE) / W	Relative difference
0.2	4.733×10^{-3}	4.731×10^{-3}	0.422×10^{-3}
0.4	8.744×10^{-3}	8.736×10^{-3}	0.915×10^{-3}
1	49.13×10^{-3}	49.04×10^{-3}	1.833×10^{-3}
5	319.1×10^{-3}	318.6×10^{-3}	1.568×10^{-3}

Table 5 Calculated values of the idler output power values for the Dy^{3+} doped chalcogenide-selenide glass fiber laser.

Pump power / W	Idler power (NU-PWr) / W	Idler power (UFE) / W	Relative difference
0.2 W	0 W	4.140×10^{-6}	NA
0.4 W	0 W	9.591×10^{-4}	NA
1 W	55.38×10^{-3} W	55.26×10^{-3}	2.169×10^{-3}
5 W	426.0×10^{-3} W	425.4×10^{-3}	1.409×10^{-3}

Table 6 Calculated values of signal output power values for the Er^{3+} ion doped fluoride glass fiber laser.

Pump power	Signal power (NU-PWr) / W	Signal power (UFE) / W	Relative difference
5 W	1.432	1.432	0
10 W	3.171	3.171	0
15 W	4.868	4.868	0
20 W	6.458	6.458	0

5. Conclusions

In the paper software packages developed within various environments for modeling and design of MIR fiber lasers are compared. The analysis was focused on the comparison of the CPU time and the values of the computational residual. The simulation results showed an advantage of using direct encoding of the algorithm in terms of the simulation time. Also, a comparison was carried out between the results obtained by different models. Both in the case of the Dy^{3+} doped chalcogenide-selenide step-index glass fiber and in the case of the Er^{3+} doped fluoride glass fiber lasers a very good agreement has been achieved between the results calculated using the UFE and PWr-UN models.

Author Contributions: conceptualization, S.S., F.P. and P.P.; methodology S.S., F.P. and P.P.; software, S.S., F.P., H.B., M.C.F. and P.P..; results calculation, L.S., S.S., F.P. M.C.F. and P.P..; formal analysis and validation, S.S., F.P. and P.P.; writing—original draft preparation, S.S., F.P., M.M., T.M.B., E.B., S.T and P.P.; writing—review and editing S.S., F.P., M.M., T.M.B., E.B., S.T and P.P.;.

Funding: This research received no external funding. The authors wish to thank COST Action MP1401 Advanced fibre laser and coherent source as tools for society, manufacturing and lifescience and Wrocław University of Science and Technology (statutory activity) for financial support. Pavel Peterka acknowledges also support from the Czech Science Foundation, project No. 16-13306S..

Acknowledgments: In this section you can acknowledge any support given which is not covered by the author contribution or funding sections. This may include administrative and technical support, or donations in kind (e.g., materials used for experiments).

Conflicts of Interest: The authors declare no conflict of interest. The funders had no role in the design of the study; in the collection, analyses, or interpretation of data; in the writing of the manuscript, or in the decision to publish the results.

References

1. Schneider, J.; Carbonnier, C.; Unrau, U.B. Characterization of a Ho^{3+}-doped fluoride fiber laser with a 3.9-μm emission wavelength. *Applied Optics* **1997**, *36*, 8595-8600.
2. Majewski, M.R.; Woodward, R.I.; Carreé, J.-Y.; Poulain, S.; Poulain, M.; Jackson, S.D. Emission beyond 4 μm and mid-infrared lasing in a dysprosium-doped indium fluoride InF_3 fiber. *Optics letters* **2018**, *43*, 1926-1929.
3. Maes, F.; Fortin, V.; Poulain, S.; Poulain, M.; Carrée, J.-Y.; Bernier, M.; Vallée, R. Room temperature fiber laser at 3.92 μm. *arXiv preprint arXiv:1804.08610* **2018**.
4. Písařík, M.; Peterka, P.; Aubrecht, J.; Cajzl, J.; Benda, A.; Mareš, D.; Todorov, F.; Podrazký, O.; Honzátko, P.; Kašík, I. Thulium-doped fibre broadband source for spectral region near 2 micrometers. *Opto-Electronics Review* **2016**, *24*, 223-231.
5. Tokita, S.; Murakami, M.; Shimizu, S.; Hashida, M.; Sakabe, S. Liquid-cooled 24 W mid-infrared Er:ZBLAN fiber laser. *Optics Letters* **2009**, *34*, 3062-3064.
6. Henderson-Sapir, O.; Jackson, S.D.; Ottaway, D.J. Versatile and widely tunable mid-infrared erbium doped ZBLAN fiber laser. *Optics Letters* **2016**, *41*, 1676-1679.

Peer-reviewed version available at *Photonics* **2018**, *5*, 48; doi:10.3390/photonics5040048

7. Henderson-Sapir, O.; Malouf, A.; Bawden, N.; Munch, J.; Jackson, S.D.; Ottaway, D.J. Recent advances in 3.5 µm erbium-doped mid-infrared fiber lasers. *IEEE Journal of Selected Topics in Quantum Electronics* **2017**, *23*.
8. Henderson-Sapir, O.; Munch, J.; Ottaway, D.J. New energy-transfer upconversion process in Er^{3+} :Zblan mid-infrared fiber lasers. *Optics Express* **2016**, *24*, 6869-6883.
9. Malouf, A.; Henderson-Sapir, O.; Gorjan, M.; Ottaway, D.J. Numerical modeling of 3.5 µm dual-wavelength pumped erbium-doped mid-infrared fiber lasers. *IEEE Journal of Quantum Electronics* **2016**, *52*.
10. Lamrini, S.; K. Scholle; Schäfer, M.; Fuhrberg, P.; Ward, J.; Francis, M.; Sujecki, S.; A. Oladeji; Napier, B.; Seddon, A.B., *et al.* High-energy Q-switched Er:ZBLAN fibre laser at 2.79 µm. In *CLEO/Europe-EQEC OSA*, OSA: Munich, Germany, 2015.
11. Li, J.F.; Jackson, S.D. Numerical modeling and optimization of diode pumped heavily-erbium-doped fluoride fiber lasers. *IEEE Journal of Quantum Electronics* **2012**, *48*, 454-464.
12. Majewski, M.R.; Jackson, S.D. Highly efficient mid-infrared dysprosium fiber laser. *Optics Letters* **2016**, *41*, 2173-2176.
13. Sakr, H.; Furniss, D.; Tang, Z.; Sojka, L.; Moneim, N.A.; Barney, E.; Sujecki, S.; Benson, T.M.; Seddon, A.B. Superior photoluminescence (pl) of Pr^{3+}-In, compared to Pr^{3+}-Ga, selenide-chalcogenide bulk glasses and PL of optically-clad fiber. *Optics Express* **2014**, *22*, 21236-21252.
14. Sakr, H.; Tang, Z.Q.; Furniss, D.; Sojka, L.; Sujecki, S.; Benson, T.M.; Seddon, A.B. Promising emission behavior in Pr^{3+}/In selenide-chalcogenide-glass small-core step index fiber (sif). *Optical Materials* **2017**, *67*, 98-107.
15. Seddon, A.B.; Furniss, D.; Tang, Z.Q.; Sojka, L.; Benson, T.M.; Caspary, R.; Sujecki, S.; Ieee. True mid-infrared Pr^{3+} absorption cross-section in a selenide-chalcogenide host-glass. In *2016 18th international conference on transparent optical networks*, 2016.
16. Seddon, A.B.; Tang, Z.; Furniss, D.; Sujecki, S.; Benson, T.M. Progress in rare-earth-doped mid-infrared fiber lasers. *Optics Express* **2010**, *18*, 26704-26719.
17. Sojka, L.; Tang, Z.; Furniss, D.; Sakr, H.; Beres-Pawlik, E.; Seddon, A.B.; Benson, T.M.; Sujecki, S. Numerical and experimental investigation of mid-infrared laser action in resonantly pumped Pr^{3+} doped chalcogenide fibre. *Optical and Quantum Electronics* **2017**, *49*.
18. Sojka, L.; Tang, Z.; Furniss, D.; Sakr, H.; Fang, Y.; Beres-Pawlik, E.; Benson, T.M.; Seddon, A.B.; Sujecki, S. Mid-infrared emission in Tb^{3+}-doped selenide glass fiber. *Journal of the Optical Society of America B-Optical Physics* **2017**, *34*, A70-A79.
19. Sojka, L.; Tang, Z.; Furniss, D.; Sakr, H.; Oladeji, A.; Beres-Pawlik, E.; Dantanarayana, H.; Faber, E.; Seddon, A.B.; Benson, T.M., *et al.* Broadband, mid-infrared emission from Pr^{3+} doped geasgase chalcogenide fiber, optically clad. *Optical Materials* **2014**, *36*, 1076-1082.
20. Sojka, L.; Tang, Z.; Zhu, H.; Beres-Pawlik, E.; Furniss, D.; Seddon, A.B.; Benson, T.M.; Sujecki, S. Study of mid-infrared laser action in chalcogenide rare earth doped glass with Dy^{3+}, Pr^{3+} and Tb^{3+}. *Optical Materials Express* **2012**, *2*, 1632-1640.

21. Tang, Z.; Furniss, D.; Fay, M.; Sakr, H.; Sojka, L.; Neate, N.; Weston, N.; Sujecki, S.; Benson, T.M.; Seddon, A.B. Mid-infrared photoluminescence in small-core fiber of praseodymium-ion doped selenide-based chalcogenide glass. *Optical Materials Express* **2015**, *5*, 870-886.
22. Tang, Z.; Neate, N.C.; Furniss, D.; Sujecki, S.; Benson, T.M.; Seddon, A.B. Crystallization behavior of Dy^{3+}-doped selenide glasses. *Journal of Non-Crystalline Solids* **2011**, *357*, 2453-2462.
23. Tang, Z.Q.; Furniss, D.; Fay, M.; Sakr, H.; Sojka, L.; Neate, N.; Weston, N.; Sujecki, S.; Benson, T.M.; Seddon, A.B. Mid-infrared photoluminescence in small-core fiber of praseodymium-ion doped selenide-based chalcogenide glass. *Optical Materials Express* **2015**, *5*, 870-886.
24. Tang, Z.Q.; Shiryaev, V.S.; Furniss, D.; Sojka, L.; Sujecki, S.; Benson, T.M.; Seddon, A.B.; Churbanov, M.F. Low loss Ge-As-Se chalcogenide glass fiber, fabricated using extruded preform, for mid-infrared photonics. *Optical Materials Express* **2015**, *5*, 1722-1737.
25. Churbanov, M.F.; Scripachev, I.V.; Shiryaev, V.S.; Plotnichenko, V.G.; Smetanin, S.V.; Kryukova, E.B.; Pyrkov, Y.N.; Galagan, B.I. Chalcogenide glasses doped with Tb, Dy and Pr ions. *Journal of Non-Crystalline Solids* **2003**, *326*, 301-305.
26. Karaksina, E.V.; Shiryaev, V.S.; Churbanov, M.F.; Anashkina, E.A.; Kotereva, T.V.; Snopatin, G.E. Core-clad Pr^{3+}-doped Ga(in)-Ge-As-Se-(i) glass fibers: Preparation, investigation, simulation of laser characteristics. *Optical Materials* **2017**, *72*, 654-660.
27. Karaksina, E.V.; Shiryaev, V.S.; Kotereva, T.V.; Churbanov, M.F. Preparation of high-purity Pr^{3+} doped Ge-Ga-Sb-Se glasses with intensive middle infrared luminescence. *Journal of Luminescence* **2016**, *170*, 37-41.
28. Shiryaev, V.S.; Karaksina, E.V.; Kotereva, T.V.; Churbanov, M.F.; Velmuzhov, A.P.; Sukhanov, M.V.; Ketkova, L.A.; Zernova, N.S.; Plotnichenko, V.G.; Koltashev, V.V. Preparation and investigation of Pr^{3+}-doped Ge-Sb-Se-In-I glasses as promising material for active mid-infrared optics. *Journal of Luminescence* **2017**, *183*, 129-134.
29. Quimby, R.S.; Shaw, L.B.; Sanghera, J.S.; Aggarwal, I.D. Modeling of cascade lasing in dy : Chalcogenide glass fiber laser with efficient output at 4.5 μm. *IEEE Photonics Technology Letters* **2008**, *20*, 123-125.
30. Sanghera, J.S.; Shaw, L.B.; Aggarwal, I.D. Chalcogenide glass-fiber-based mid-ir sources and applications. *IEEE Journal of Selected Topics in Quantum Electronics* **2009**, *15*, 114-119.
31. Shaw, L.B.; Cole, B.; Thielen, P.A.; Sanghera, J.S.; Aggarwal, I.D. Mid-wave ir and long-wave ir laser potential of rare-earth doped chalcogenide glass fiber. *IEEE Journal of Quantum Electronics* **2001**, *37*, 1127-1137.
32. Falconi, M.C.; Palma, G.; Starecki, F.; Nazabal, V.; Troles, J.; Adam, J.L.; Taccheo, S.; Ferrari, M.; Prudenzano, F. Dysprosium-doped chalcogenide master oscillator power amplifier (MOPA) for mid-ir emission. *Journal of Lightwave Technology* **2017**, *35*, 265-273.

Peer-reviewed version available at Photonics 2018, 5, 48; doi:10.3390/photonics5040048

33. Falconi, M.C.; Palma, G.; Starecki, F.; Nazabal, V.; Troles, J.; Taccheo, S.; Ferrari, M.; Prudenzano, F. Design of an efficient pumping scheme for Mid-IR Dy^{3+}:$Ga_5Ge_{20}Sb_{10}S_{65}$ PCF fiber laser. *IEEE Photonics Technology Letters* **2016**, *28*, 1984-1987.
34. Moizan, V.; Nazabal, V.; Troles, J.; Houizot, P.; Adam, J.-L.; Doualan, J.-L.; Moncorge, R.; Smektala, F.; Gadret, G.; Pitois, S., *et al.* Er^{3+}-doped gegasbs glasses for mid-ir fibre laser application: Synthesis and rare earth spectroscopy. *Optical Materials* **2008**, *31*, 39-46.
35. Pele, A.L.; Braud, A.; Doualan, J.L.; Starecki, F.; Nazabal, V.; Chahal, R.; Boussard-Pledel, C.; Bureau, B.; Moncorge, R.; Camy, P. Dy^{3+} doped gegasbs fluorescent fiber at 4.4 μm for optical gas sensing: Comparison of simulation and experiment. *Optical Materials* **2016**, *61*, 37-44.
36. Starecki, F.; Morais, S.; Chahal, R.; Boussard-Pledel, C.; Bureau, B.; Palencia, F.; Lecoutre, C.; Garrabos, Y.; Marre, S.; Nazabal, V. IR emitting Dy^{3+} doped chalcogenide fibers for in situ co_2 monitoring in high pressure microsystems. *International Journal of Greenhouse Gas Control* **2016**, *55*, 36-41.
37. Sujecki, S. An efficient algorithm for steady state analysis of fibre lasers operating under cascade pumping scheme. *Intl. Journal of Electronics and Telecommunications* **2014**, *60*, 143-149
38. Sujecki, S. Numerical analysis of q-switched erbium ion doped fluoride glass fiber laser operation including spontaneous emission. *Applied Sciences* **2018**, *8*, 803.
39. Sujecki, S.; Sojka, L.; Beres-Pawlik, E.; Tang, Z.; Furniss, D.; Seddon, A.B.; Benson, T.M. Modelling of a simple Dy^{3+} doped chalcogenide glass fibre laser for mid-infrared light generation. *Optical and Quantum Electronics* **2010**, *42*, 69-79.
40. Falconi, M.C.; Palma, G.; Starecki, F.; Nazabal, V.; Troles, J.; Adam, J.L.; Taccheo, S.; Ferrari, M.; Prudenzano, F.; IEEE. Novel pumping schemes of mid-ir photonic crystal fiber lasers for aerospace applications. In *2016 18th international conference on transparent optical networks*, 2016.
41. Peterka, P.; Koška, P.; Čtyroký, J. Reflectivity of superimposed bragg gratings induced by longitudinal mode instabilities in fiber lasers. *IEEE Journal of Selected Topics in Quantum Electronics* **2018**, *24*, 1-8.
42. Falconi, M.C.; Palma, G.; Starecki, F.; Nazabal, V.; Troles, J.; Adam, J.L.; Taccheo, S.; Ferrari, M.; Prudenzano, F. Recent advances on pumping schemes for Mid-IR PCF lasers. In *Optical components and materials xiv*, Jiang, S.; Digonnet, M.J.F., Eds. 2017; Vol. 10100.